ELSEVIER

International Journal of Heat and Fluid Flow 21 (2000) 655–663

International Journal of
HEAT AND FLUID FLOW

www.elsevier.com/locate/ijhff

Large-eddy simulation of separated flow over a bluff rectangular plate

A. Suksangpanomrung [a], N. Djilali [a,*], P. Moinat [b]

[a] Department of Mechanical Engineering, University of Victoria, Victoria, BC, Canada V8W 3P6
[b] CERFACS, 31057 Toulouse Cedex 1, France

Abstract

The turbulent separated-reattaching flow over a bluff rectangular plate is investigated using the large-eddy simulation (LES) technique. Simulations are presented for a Reynolds number (Re_d) of 50,000 and a blockage ratio (Br) of 5.6%. Three subgrid-scale models are used: structure function, selective structure function and Smagorinsky models. The performance of these models is examined by comparing the mean flow and turbulence statistics, and the dynamics of the flow with experimental observations. With both structure-function and Smagorinsky models, the break-up and three-dimensionalization of the separated shear layer are delayed. The dynamics of the reattaching flow is altered by the persistence of small-scale structures in the Smagorinsky model simulation, while excessive subgrid-scale dissipation is evident in the structure function simulation. Both models yield deficient mean flow structures and turbulence statistics. The selective version of the structure function model, which allows a localization of the subgrid-scale contribution, produces separated shear layer instabilities, dynamical patterns, and structures which are physically consistent with flow visualization. The mean flow and turbulent statistics obtained with this model are also found to be in excellent agreement with measurements. Using structure identification techniques based on the vorticity modulus $|\omega|$ and the eigenvalue λ_2 of the tensor $S_{ik}S_{kj} + \Omega_{ik}\Omega_{kj}$, horseshoe vortices hypothesized in earlier experimental work are clearly identified in the reattachment region. Wavelet signal analysis reveals the persistence of scales associated with shear layer flapping and the intermittent nature of the pseudo-periodic shedding of vortices in the reattachment region. © 2000 Begell House Inc. Published by Elsevier Science Inc. All rights reserved.

Keywords: Separated-reattaching flow; Large-eddy simulation; Subgrid-scale models; Coherent structures; Wavelet analysis

1. Introduction

Flows with large regions of separation occur in a variety of environmental and engineering applications. Large-scale unsteadiness, complex turbulent structure, curvature effects and large pressure gradients characterize these flows. Many of these features have been challenging to predict using Reynolds-averaged turbulence models. In this paper, we investigate the unsteady separated-reattaching flow around a bluff rectangular plate using the large-eddy simulation (LES) technique. This “benchmark” bluff plate geometry, which is relevant to heat exchanger applications and is shown in Fig. 1, simplifies considerably the study of separated-reattaching flows: the location of separation is fixed; the shear layer at separation is thin; and the upstream boundary conditions are simple and well defined. This eliminates the need for a prohibitively large upstream computational domain to allow the development of upstream profiles with the correct turbulence characteristics. Also, for a sufficiently long plate, the separated shear layers on the top and bottom of the plate reattach to the surface and do not interact.

The mean flow characteristics and large-scale unsteadiness aspects of turbulent flow around a bluff rectangular plate have been the subject of a number of experimental studies at high Reynolds numbers ($\geqslant$ 20,000) (e.g., Cherry et al., 1983; Kiya and Sasaki, 1983; Djilali and Gartshore, 1991a; Saathoff and Melbourne, 1997). All studies report a characteristic low frequency flapping of the separated shear layer as well as pseudo-periodic vortex shedding from the separation bubble. The strong dependence of the flow on free stream turbulence is well documented (Hillier and Cheery, 1981; Saathoff and Melbourne, 1997). A reduction of over 50% in the mean reattachment length ($\overline{X}_r$) and significant changes in the dynamics of the flow and spanwise length scales have been reported when high levels of turbulence (of the order of 12%) are introduced in the free stream.

Numerical studies of the unsteady separated flow over a bluff plate are scarce. The direct numerical simulation of Tafti and Vanka (1991) was confined to the transitional regime at a low Reynolds number of 1000, but nonetheless reproduced many of the large-scale characteristics observed at higher Reynolds numbers. Reynolds-averaged Navier–Stokes (RANS) of the high Reynolds number turbulent flow (Djilali and Gartshore, 1991b) have provided an adequate representation of the mean flow characteristics within the separation bubble. However ad hoc modifications of the turbulence model were required, and, even then, a marked deterioration of the

---

* Corresponding author. Tel.: +1-250-7216034; fax: +1-250-7216051.
E-mail address: ndjilali@uvic.ca (N. Djilali).

PII: S0142-727X(00)00057-6

Notations

Br	blockage ratio, $Br = d/H$
d	thickness of the plate
fd/U_0	non-dimensional frequency unit
H	height of the computational domain/flow channel
L_d	distance to the outlet boundary from the separation point
L_u	distance to the inlet boundary from the separation point
L_z	spanwise dimension
Re_d	Reynolds number based on thickness of the plate, $Re_d = U_0 d/\nu$
u_i	instantaneous velocity components
$\langle u' \rangle$	root mean square of streamwise velocity fluctuation
$-\langle u'v' \rangle$	root mean square of turbulent shear stress
U_0	free stream velocity
$\underline{x_i}$	Cartesian coordinate (x, y and z)
$\overline{X}_\mathrm{r}$	mean (time and spanwise-averaged) reattachment length
t	time
tU_0/d	non-dimensional time unit
λ_2	the second largest eigenvalues
ν	kinematic molecular viscosity
ν_t	kinematic turbulent (eddy) viscosity
ω	vorticity

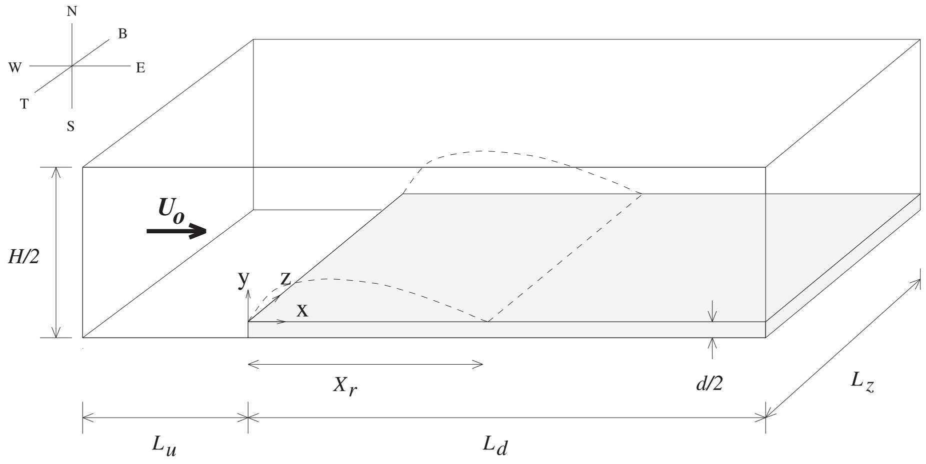

Fig. 1. Computational domain, $L_u = 4d, L_d = 12d, L_z = 5.2d, d/H = 0.056$.

predictions in the recovery region was noted. Furthermore, such RANS computations cannot provide information on the complex dynamics of the flow and on the large-scale unsteadiness that dominate turbulent transport. To investigate these features and provide a detailed description of the turbulent transport, LESs at a Reynolds number of 50,000 are presented in this paper.

2. Computational method

2.1. Mathematical Model

The governing equations for the large-scale (resolved) motion can be obtained by applying a spatial filter (indicated by an overbar) to both the continuity and the Navier–Stokes equations, with the result (Ferziger, 1993; Lesieur and Métais, 1996)

$$\frac{\partial \bar{u}_i}{\partial x_i} = 0, \tag{1}$$

$$\frac{\partial \bar{u}_i}{\partial t} + \frac{\partial \bar{u}_i \bar{u}_j}{\partial x_j} = -\frac{1}{\rho}\frac{\partial \bar{p}}{\partial x_i} + \nu \frac{\partial^2 \bar{u}_i}{\partial x_j^2} + \frac{\partial T_{ij}}{\partial x_j}, \tag{2}$$

where the subgrid-scale tensor $T_{ij} = \bar{u}_i \bar{u}_j - \overline{u_i u_j}$, which represents the lumped effect of the subgrid-scales on the resolved scales, is modelled using an eddy-viscosity assumption

$$T_{ij} = \nu_\mathrm{t}\left(\frac{\partial \bar{u}_i}{\partial x_j} + \frac{\partial \bar{u}_j}{\partial x_i}\right) + \frac{1}{3} T_{kk}\delta_{ij}. \tag{3}$$

In this study, the eddy viscosity (ν_t) is evaluated using three subgrid-scale (SGS) models: the structure function (SF), selective structure function (SSF) and Smagorinsky models (SM). In the structure function model, the eddy viscosity is evaluated according to (Lesieur and Métais, 1996)

$$\nu_\mathrm{t}(x, \Delta_c, t) = 0.063 \Delta_c \sqrt{\overline{F}_2(\mathbf{x}, \Delta_c, t)}, \tag{4}$$

where Δ_c is the mean mesh size, and $\overline{F}_2$ is the second-order structure function of the resolved velocity field for a radius Δ_c,

$$\overline{F}_2(\mathbf{x}, \Delta_c, t) = \langle \|\bar{\mathbf{u}}(\mathbf{x}+\mathbf{r}, t) - \bar{\mathbf{u}}(\mathbf{x}, t)\|^2 \rangle_{\|\mathbf{r}\| = \Delta_c}. \tag{5}$$

In the selective version of the structure function model given by

$$\nu_\mathrm{t}(x, \Delta_c, t) = 0.098 \zeta \Delta_c \sqrt{\overline{F}_2(\mathbf{x}, \Delta_c, t)}, \tag{6}$$

better localization of the small-scale turbulence is achieved by switching off the eddy viscosity ($\zeta = 0$) when the flow is not sufficiently three-dimensional. The measure of three-dimensionality used to determine the value of the selectivity parameter ζ is the angle β between the local vorticity vector and the average vorticity over the neighbouring points. A threshold value of 20° for β is recommended by Lesieur and Métais for switching on–off the eddy viscosity. This corresponds to the most probable angle obtained from LES of isotropic turbulence. In the present study, rather than using an abrupt on–off switch, ζ is evaluated using a smoothly varying function

$$\zeta = \begin{cases} 0 & \text{for } \beta < 10^\circ, \\ e^{-(d\beta/3)^2} & \text{for } 20^\circ \geqslant \beta \geqslant 10^\circ \text{ and } d\beta = |\beta - 20|, \\ 1 & \text{for } \beta > 20^\circ. \end{cases} \tag{7}$$

The third SGS model investigated, the Smagorinsky model, is implemented with a damping function (see Kogaki et al., 1997)

$$\nu_t(x, \Delta_c, t) = (0.13 D\Delta_c)^2 (2\bar{S}_{ij}\bar{S}_{ij})^{1/2}, \tag{8}$$

where D is the Damping function, $D = 1 - e^{-y^+/A}$, and $\bar{S}_{ij}$ is the strain rate, $\bar{S}_{ij} = \frac{1}{2}(\partial\bar{u}_i/\partial x_j + \partial\bar{u}_j/\partial x_i)$.

2.2. Numerical method

A staggered grid, finite volume method is employed. Mixed discretization is adopted in the computational domain, i.e., second-order central differencing (CD) is used downstream of the leading edge of the plate to ensure that the simulations in the zone of interest are free from numerical dissipation and a quadratic upwind scheme (QUICK) is used in the region upstream of the plate to avoid the generation of spurious oscillations in the high gradient region immediately upstream of the leading corner of the plate. This procedure was adopted following a preliminary investigation of Suksangpanomrung et al. (1997), in which small perturbations arising from the use of the unbounded CD scheme in the upstream region were found to have an effect similar to increased free stream turbulence.

A third order Runge–Kutta algorithm is used for time integration in conjunction with a classical correction method at each substep. The continuity equation (1) and the pressure gradient term in the momentum (2) are treated implicitly, while the convective and diffusive terms are treated explicitly. The linear system for pressure is solved by an efficient conjugate gradient method with preconditioning. Further details on the numerical method are given in Suksangpanomrung (1999).

2.3. Computational domain and boundary conditions

A schematic of the flow domain, coordinate system and key-dimensional parameters are shown in Fig. 1. The simulations were performed at a Reynolds number (Re_d) of 50,000 and for a blockage ratio (Br) of 5.6%. This corresponds to the conditions used in the experimental study of Djilali and Gartshore (1991a). A computational grid of $N_x \times N_y \times N_z = 108 \times 61 \times 27$ is used, with non-uniform distributions in the x and y directions, and with the finest grid spacing of order $0.01d$ located around the leading edge of the plate. A uniform grid is used in the spanwise direction with a spacing of $\Delta z = 0.2d$.

In the reference experimental flow, the background turbulence in the free stream was low ($\approx 0.25\%$) and the velocity profile at the inlet of the test section uniform within 1%. Uniform flow is therefore imposed at the inlet of the computational domain, and no attempt is made to introduce free stream turbulence by perturbing the inlet profile.

At the outlet, an advective condition is imposed via $\partial u/\partial t + C_u \partial u/\partial x = 0$, where C_u is taken as the time-averaged bulk velocity. A series of preliminary two- and three-dimensional computations were performed to determine the effect of the downstream extent of the computational domain, L_d, in conjunction with the advective outlet condition. A difference of less than 1% was found for the mean reattachment length when L_d was shortened from $20d$ to $12d$; the latter value was therefore used in all present simulations.

A periodic boundary condition is imposed in the spanwise direction. The extent of the domain L_z in this direction is over twice the spanwise correlation length obtained experimentally by Saathoff and Melbourne (1997). Symmetry is imposed along the lower boundary upstream of the plate ($-L_u < x < 0; y = -d/2$).

The resolution of the near-wall region is impractical at the Reynolds number of 50,000 considered here, and the grid points adjacent to solid walls are typically located at $y^+ \approx 15$–30. The surface of the plate and the top boundary of the domain ($y = H/2 - d/2$) are hence treated as no-slip boundaries with an approximate wall model. The wall function formulation of Mason and Callen (1986) was adopted. Considering a near-wall grid point, we define the tangential velocity $\vec{U}_t$ as the projection of the velocity vector at this point onto a plane parallel to the wall, and U_t as the modulus of this velocity vector. Depending on the value of $y^+ = U_t y/\nu$, the friction velocity is determined locally and instantaneously from: $U^+ = y^+$ for $y^+ < 3$, $U^+ = 2.4\ln(y^+) + 5$ for $y^+ > 200$, or from a tabulated connecting law in between. The wall shear stress is then deduced by assuming it acts in a direction parallel to $\vec{U}_t$. Though the validity of this approach is not generally verified, nor always adequate, such type of near-wall treatment is currently unavoidable at high Reynolds numbers.

3. Results and discussion

3.1. Mean flow characteristics

The mean (time and spanwise-averaged) reattachment lengths, $\overline{X}_r$, obtained with the three SGS models are given in Table 1. The time step is varied and constrained by the CFL condition, and is of the order of 0.006 tU_0/d for the structure functiion (3DSF) and Smagorinsky model (3DSM) and 0.003 tU_0/d for the selective structure function (3DSSF). Simulations over an initial "start-up" period of about 50 tU_0/d were discarded to allow the passage of initial transients. Subsequently, all simulations were integrated over 400 tU_0/d (about 35 "residence" times). The spanwise and time-averaged streamline patterns from all three simulations are compared with experiments in Fig. 2. Although 3DSM provides the best prediction of $\overline{X}_r$, the streamline pattern compared to experiments is skewed, with the location of the center of the mean recirculating vortex located too far downstream, and a lifting of the streamlines away from the wall in the first half of the bubble. The mean flow pattern of 3DSSF provides better overall agreement with experiments, and both the shape and the location of the center of recirculation are well predicted.

Fig. 3 compares predicted mean surface pressure distributions along the surface of the plate. The experimental trend is reproduced reasonably well by all three simulations. The minimum mean surface pressure coefficients are

Table 1
Mean reattachment length and sampling time for the three simulations with comparison to experimental data

Simulation	SGS model	Integrating times (tU_0/d)	$\overline{X}_r/d$
3DSF	SF	400	5.14
3DSSF	SSF	400	4.30
3DSM	SM	400	4.57
Djilali and Gartshore (1991a)	Expt.	–	4.7 ± 0.1

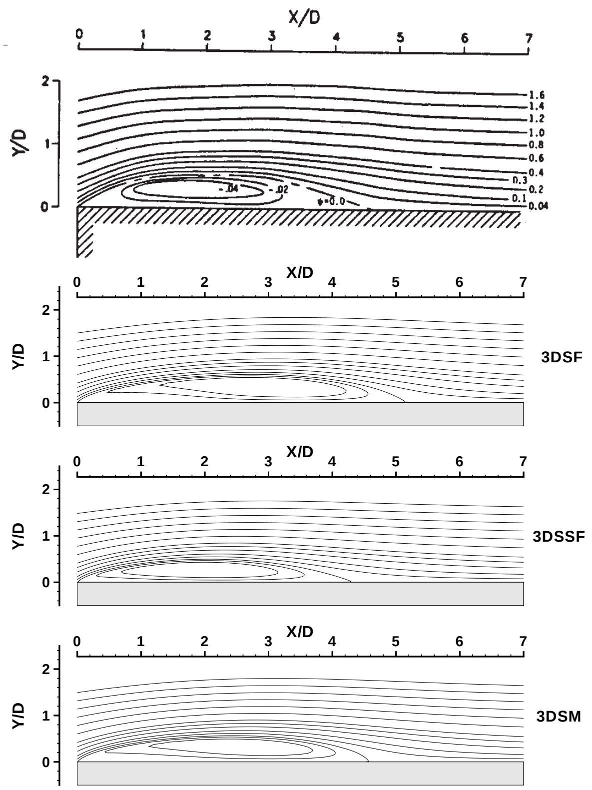

Fig. 2. Mean streamline patterns.

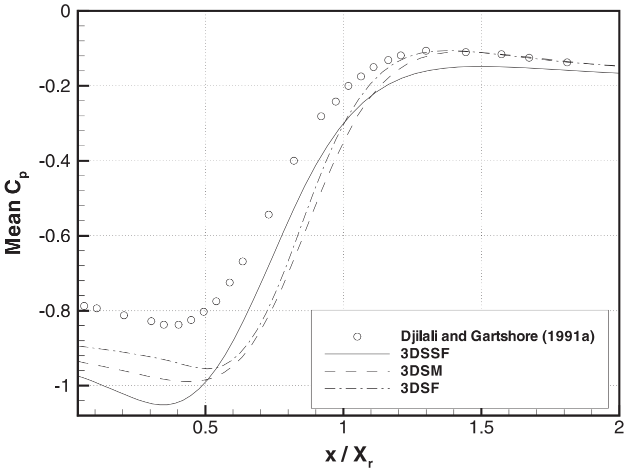

Fig. 3. Mean surface pressure coefficient distributions.

underpredicted by about 10–18%, depending on the SGS models, however 3DSSF provides better agreement for the location of the minimum at $x/\overline{X}_r \approx 0.375$ and the recovery rate afterwards. The strength and location of the surface pressure minima is coupled with the vorticity in the mean separation bubble. The recovery process for all three SGS simulations is completed by $x/\overline{X}_r \approx 1.35$, which is identical to experimental observations. Downstream of the recovery region ($x/\overline{X}_r \gtrsim 1.35$), the flow is dominated by the redeveloping boundary layer which takes place under a slightly negative streamwise pressure gradient. We note a slight underprediction of the surface pressure coefficient of 3DSSF in this region. Fig. 4 compares simulated and measured wall shear stress distributions. Again, the experimental trends are well reproduced and the maxima and minima compare well within the large uncertainty band of the experimental shear stress (±25%).

Fig. 5 compares the mean streamwise velocity profiles at several stations along the plate with pulsed-wire measurements. The 3DSSF profiles are in very good agreement with measurements at all stations, but both 3DSF and 3DSM predict a broader backflow profile and underestimate the peak backflow velocity over the first half of the separation bubble. Further downstream, the three simulations yield similar profiles. In the recovery region, the present LES simulations do not suffer from the commonly observed velocity defect obtained with RANS computations (Djilali and Gartshore, 1991b). The dynamics of the flow in this region is largely governed by the large-scale unsteadiness, a process that is well captured by LES but poorly modelled in RANS-based calculations.

The mean turbulent intensity profiles, including both resolved and SGS contributions, are presented in Fig. 6. The subgrid-scale contribution to the turbulent shear stress is obtained directly from the simulations via Eq. (3). For the longitudinal normal stress, the approximation of Silveira et al. (1993) is used to evaluate the trace T_{kk} in Eq. (3). The 3DSSF

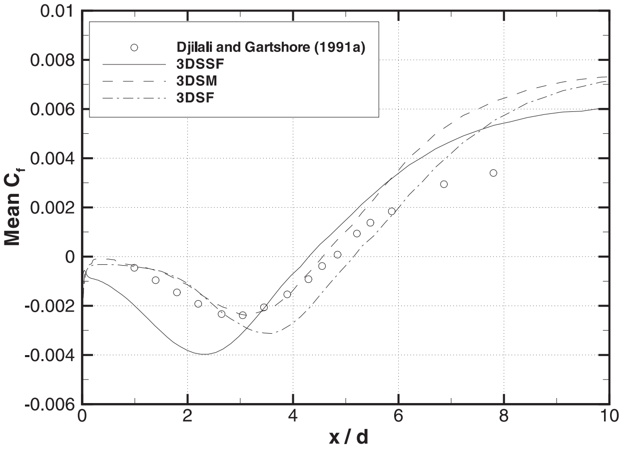

Fig. 4. Mean wall shear stress coefficient distributions.

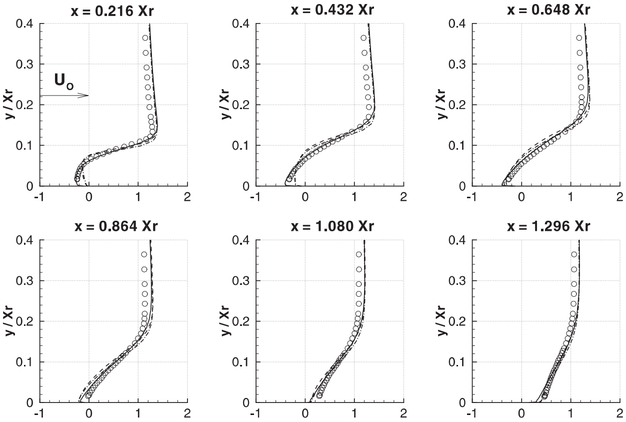

Fig. 5. Mean streamwise velocity (u/U_0) profiles at selected locations: Experimental (Djilali and Gartshore, 1991a), (○); 3DSSF (——), 3DSM (– – – –), 3DSF (· – · – ·).

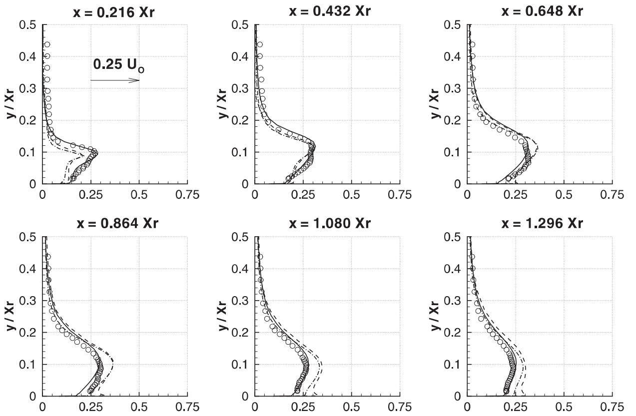

Fig. 6. Mean streamwise turbulent intensity ($\langle u' \rangle / U_0$) profiles: Experimental (Djilali and Gartshore, 1991a), (◯); 3DSSF (——), 3DSM (– – – –), 3DSF (· – · – ·).

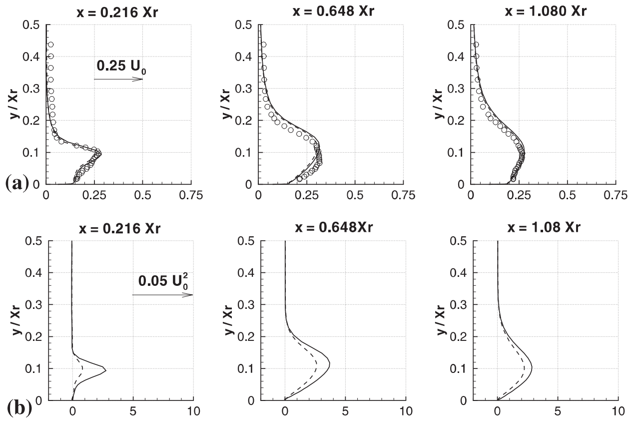

Fig. 7. Contribution of the 3DSSF SGS model to (a) the streamwise turbulent intensity, (b) the turbulent shear stress: Experimental (Djilali and Gartshore, 1991a), (◯); Total (——), Resolved (– – – –).

simulation yields remarkably good agreement with experimental data throughout. The cusp near the leading edge is well reproduced, the correct evolution of the maximum intensities with streamwise direction is obtained and a maximum value of $\langle u' \rangle / U_0 \approx 0.3$ is attained in the last third of the mean separation bubble. The 3DSF and 3DSM profiles, on the other hand, have noticeable deficiencies. The intensities are underestimated for $x/\overline{X}_r < 0.4$, and are overestimated for $x/\overline{X}_r > 0.5$. In 3DSM, where wall damping is used, a near-wall peak is present after $x/\overline{X}_r > 0.6$. Available measurements do not resolve the near-wall region, but the appearance of a near-wall peak in the recovery region, $x/\overline{X}_r > 1.2$, is not unrealistic. Such a feature was reported in the highly resolved DNS of the low Reynolds number flow over a backward facing step of Le et al. (1998).

The contribution of the SGS to the mean turbulent intensity ($\langle u' \rangle / U_0$) and the mean turbulent shear stress ($-\langle u'v' \rangle / U_0$) is shown in Fig. 7 at selected locations for the 3DSSF case. The contribution is generally largest close to the separation point, where the rapid break-up of the two-dimensional structures occurs, right after the leading edge. The SGS contribution to $-\langle u'v' \rangle / U_0$ component in Fig. 7(b) is significant, especially in the vicinity of separation. In 3DSF, the contribution of the model to both components is similar to the 3DSSF, whereas in the Smagorinsky model (3DSM), the SGS contribution is minimal. The dissipation provided by this model is, in the mean, very small and confined to the early part of the separated shear layer. It should be noted that the constant used here is that recommended by Kogaki et al. (1997) for separated flow around rectangular cylinders and is lower than the "standard" value used in boundary layer simulations. The mean subgrid-scale eddy viscosities produced by each model are shown in Fig. 8. Both structure function models (3DSSF and 3DSF) yield larger dissipation in the reattachment and recovery zones, particularly for 3DSF, and is therefore expected to have a stronger influence on the dynamics of the flow in the reattachment zone. The lower dissipation produced by

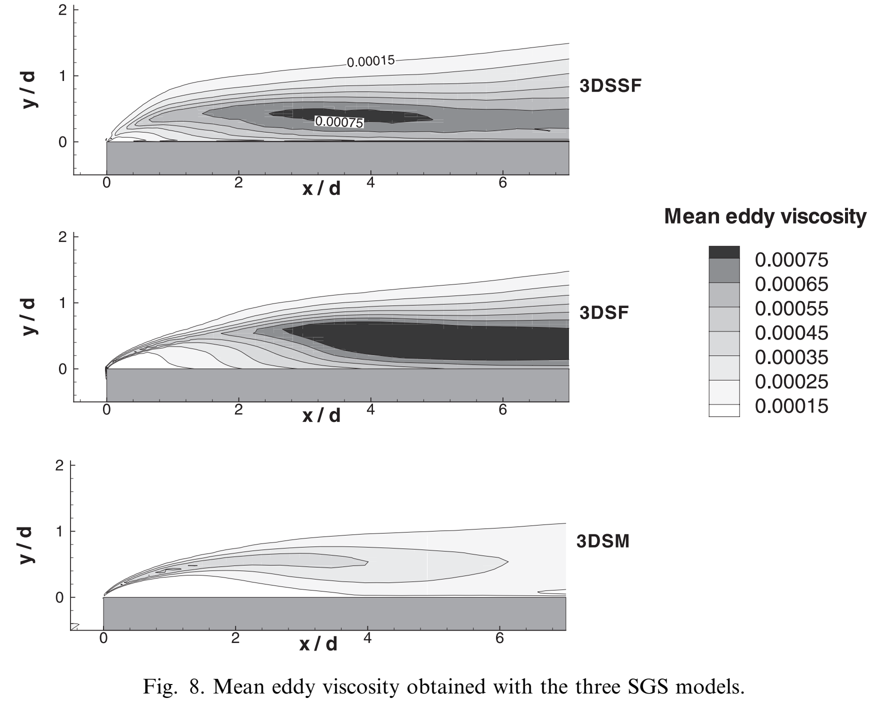

Fig. 8. Mean eddy viscosity obtained with the three SGS models.

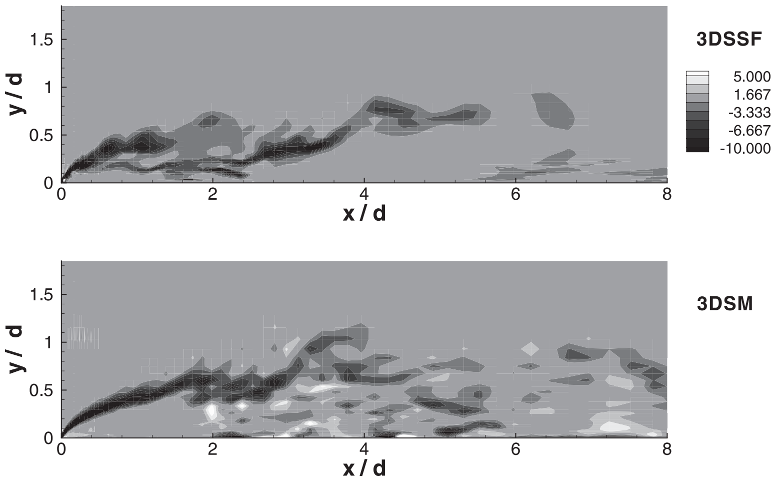

Fig. 9. Instantaneous spanwise vorticity contours in *x–y* plane at $z/d = 2.6$: 10 contours from $-10\ U_0/d$ to $5\ U_0/d$.

3DSSF near separation as a result of localization of the SGS model is also clearly illustrated.

3.2. Flow structures

Instantaneous spanwise vorticity fields from the 3DSSF and the 3DSM simulations are shown in Fig. 9. In the case of 3DSM, no significant fluctuations are detected in the separated shear layer before $x/d \approx 1.8$, whereas instabilities appear much sooner in 3DSSF. The small-scale structures are much more prominent in the reattachment region for 3DSM. This is consistent with the higher turbulent intensities obtained with this model in the reattachment and recovery regions (cf. Fig. 6), and the much lower SGS dissipation produced by the model in the reattachment zone as shown in Fig. 8. On the other hand, the higher dissipation introduced by 3DSM immediately after separation delays the break-up of the separated shear layer until the beginning of the adverse pressure gradient zone at $x/X_r \approx 0.4$.

Fig. 10 shows the instantaneous streamwise vorticity field in a plane close to the surface of the plate. 3DSM and 3DSF exhibit less "coherence" and contain smaller structures with roughly equal characteristic sizes in the spanwise and streamwise directions. The structures become gradually more elongated only after reattachment. 3DSSF exhibits a much higher degree of coherence and structures with streamwise lengths in the range of $1 - 3d$ are apparent. Significant streamwise vorticity levels are not observed until well downstream of separation with the appearance of counter-rotating pairs of vortices.

Overall, the selective structure function simulation (3DSSF) produces separated shear layer instabilities, dynamical patterns, and structures that are physically consistent with the flow visualization of Saathoff and Melbourne (1997). It was also shown in the previous section that the 3DSSF mean flow characteristics are in better agreement with experimental data. Further analysis is therefore confined to the 3DSSF simulation.

The instantaneous vorticity field for 3DSSF is plotted in Fig. 11 in terms of the vorticity modulus $|\omega|$. In this figure, the structures close to separation are hardly discernible, however, three horseshoe vortices are visible in the reattachment region. In order to identify the flow structures more clearly, the technique of Jeong and Hussain (1995) was used. In this method, the vortex cores are extracted directly from the instantaneous velocity fields. The vortex cores are identified with a region of negative λ_2, the second largest eigenvalue of the tensor $S_{ik}S_{kj} + \Omega_{ik}\Omega_{kj}$, where $S_{ij} = (u_{i,j} + u_{j,i})/2$ and $\Omega_{ij} = (u_{i,j} - u_{j,i})/2$ are the symmetric and antisymmetric parts of the velocity gradient tensor, $u_{i,j} = \partial u_i/\partial x_j$. The effectiveness of this method in capturing vortical structures, even in the presence of strong shear occurring in near wall boundary layers, has been demonstrated by Jeong et al. (1997).

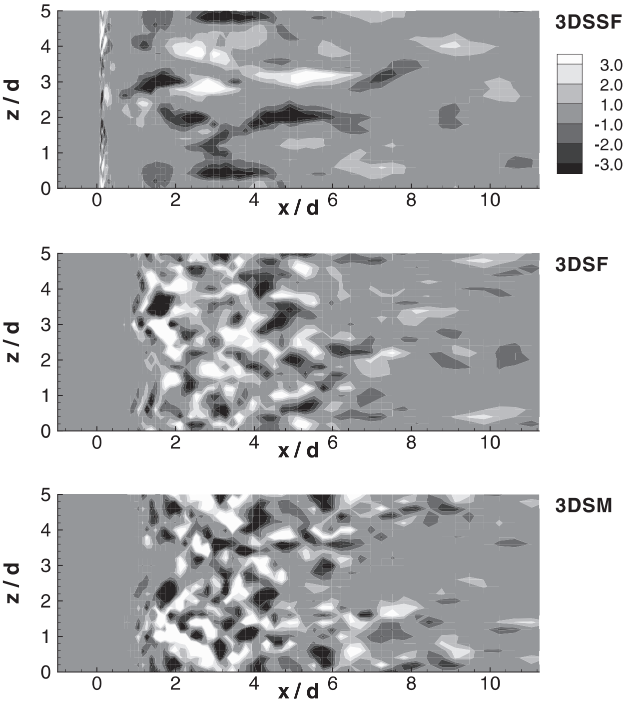

Fig. 10. Instantaneous streamwise vorticity contours in *x–z* plane at $y/d = 0.12$: 7 contours from $-3\ U_0/d$ to $3\ U_0/d$.

The contour plot of the second largest eigenvalue (λ_2) is plotted in Fig. 12 for the same instantaneous fields as Fig. 11. Structures that were barely discerned when examining the vorticity modulus are now clearly put in evidence. In the first half of the mean separation bubble, $x/d \leqslant 2$, the "noise" due to the strong background shear along the separated shear layer is eliminated and only vortex cores associated with flow structures remain. These structures are largely two-dimensional and

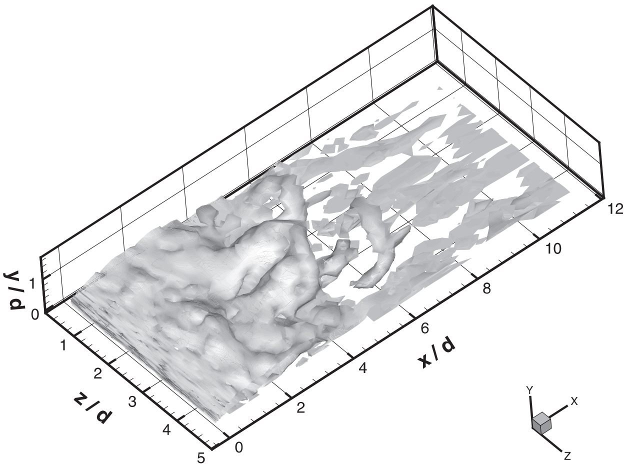

Fig. 11. Instantaneous vorticity contour: $|\omega| = 2.5\ U_0/d$ (3DSSF simulation).

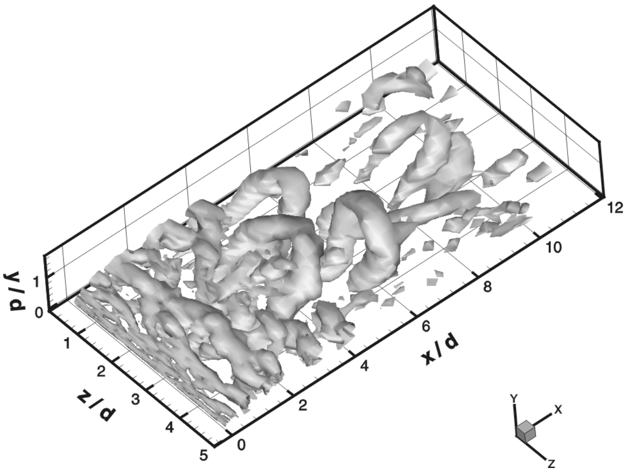

Fig. 12. Instantaneous contour plot of $\lambda_2 : \lambda_2 = -0.1$ (3DSSF simulation).

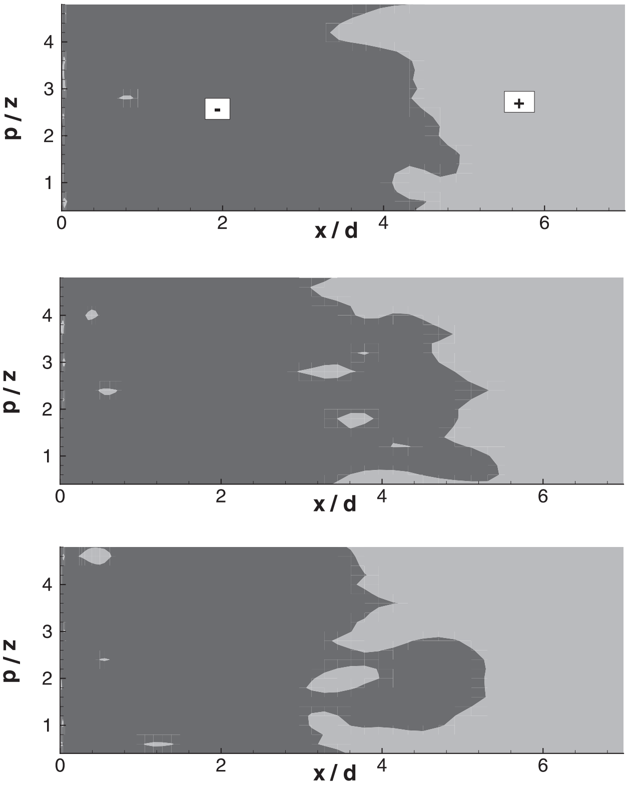

Fig. 13. Time frames illustrating the instantaneous motion of the line of reattachment in the x–z plane (3DSSF simulation). Dark/light colour indicate negative/positive wall shear stress.

develop initially at the leading edge of the plate. Further downstream, in the reattachment region, three-dimensionalization has occurred and the predominant structures are clearly identified as hairpin (horseshoe) vortices. These are identical to the sketch suggested by Kiya and Sasaki (1985) based on the interpretation of conditionally sampled data.

The spanwise length scale of the horseshoe vortices in the reattachment region range from $1.5d$ to $2.75d$ (0.35–$0.58\ \overline{X}_\mathrm{r}$), which is in the range suggested by Kiya and Sasaki (1985) and Saathoff and Melbourne (1997). The legs of the horseshoe vortices are inclined with respect to the streamwise direction. A typical vortex grows in every direction as it is advected downstream of the reattachment region. Due to the interaction between the vortical motion of the large-scale structure and the wall, it also tends to lift away from the wall. This in turn, brings the top end of the horseshoe vortex into contact with the outer (higher velocity) region, resulting in further stretching and inclination of the vortex along the flow direction. Eventually, the central portion breaks down, and only the two inclined legs remain. This phenomenon takes place in the recovery region. The unsteady motion from the shedding of these large-scale vortices causes oscillations and meandering of the instantaneous reattachment (zero-shear stress) line. Three time frames illustrating the motion of this line are shown in Fig. 13. The oscillation is apparently controlled indirectly by the flapping motion of the shear layer, or low-frequency unsteadiness (Kiya and Sasaki, 1985) which is not clearly understood and difficult to identify.

3.3. Signal analysis: 3DSSF simulation

Fig. 14(a) shows the trace of the instantaneous vertical velocity recorded just downstream of separation within the shear layer, and the corresponding power density spectrum is shown in Fig. 14(b). Consistent with the experimental spectra of Djilali and Gartshore (1991a), high frequency motion is dominant in the vicinity of separation, and the spectrum indicates small eddies with time scales of the order of $0.3\ tU_0/d$. In addition to the high-frequency activity centered around $fd/U_0 = 0.8$, the signal also exhibits peaks in the low-frequency range ($fd/U_0 \approx 0.02$–0.08). These are attributed to the flapping motion of the shear layer.

To provide further insight into the flow dynamics around the reattachment region, the streamwise velocity signal at a location close to the mean reattachment and the corresponding (Fourier) power spectrum density are presented in Fig. 15. Compared to the signal sampled near separation (Fig. 14), there is little energy in the high frequencies; most of the energy is in the larger scales corresponding to non-dimensional frequencies (fd/U_0) well below 0.2.

A time domain analysis using the wavelet transform (Farge, 1992) of the near-wall streamwise velocity signal was conducted in this region. Fig. 16 shows the wavelet map of this signal, in terms of the relief plot of the absolute value of the wavelet coefficient. The intermittent nature of the large-scale

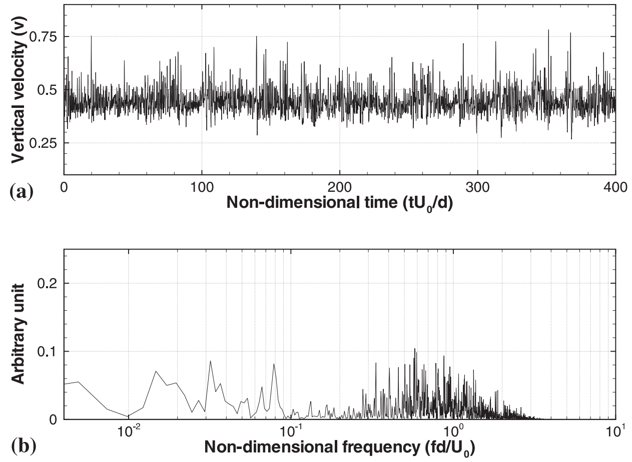

Fig. 14. 3DSSF simulation: (a) vertical velocity (v) signal at $x/d = 0.493,\ y/d = 0.47$, mid-span, (b) power spectrum density.

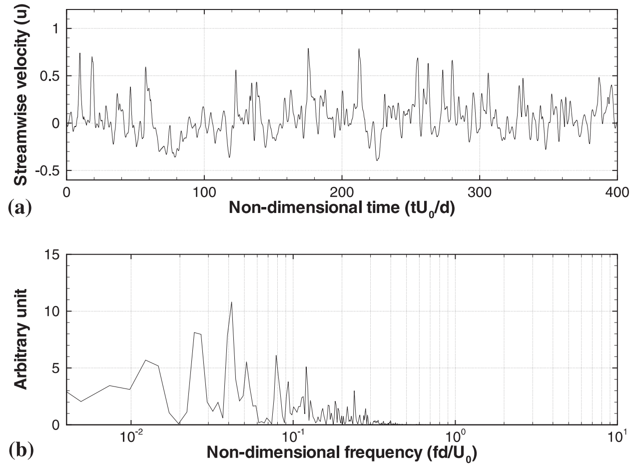

Fig. 15. 3DSSF simulation: (a) near-wall streamwise velocity (u) signal at $x/d = 4.51$, mid-span, (b) power spectrum density.

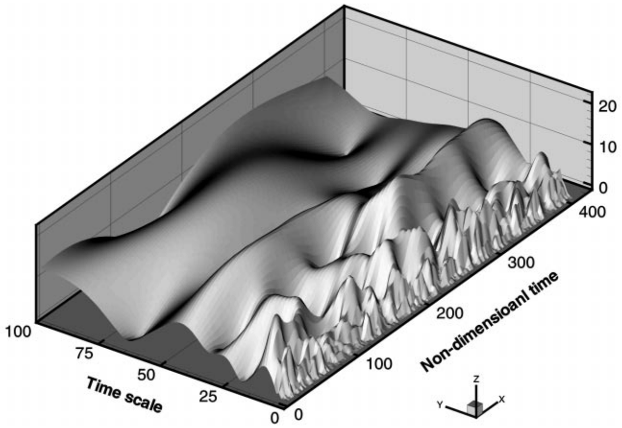

Fig. 16. Morlet wavelet map of near-wall streamwise velocity (u) signal at $x/d = 4.51$, mid-span (3DSSF simulation).

unsteadiness is illustrated along the most distinct range of scales: $tU_0/d \approx 20$–50. This range corresponds to non-dimensional frequencies of 0.02–0.05 and is associated with the low frequency flapping of the shear layer discussed earlier. The intermittency of this phenomenon is clearly shown by the alternating peaks and troughs between 45 and 395 time units. The scales containing the most energy are in the range of 5–$15tU_0/d$, or non-dimensional frequencies of 0.066–0.2. This coincides with the range of frequencies reported experimentally for the pseudo-periodic vortex shedding around reattachment (e.g., Cherry et al., 1983; Djilali and Gartshore, 1991a). The time localization of these events shows activity bursts of relatively short duration, followed by longer quiescent periods. Furthermore, the signal in Fig. 15(a) shows positive fluctuations about the mean which are of a much higher amplitude than the negative fluctuations. This feature and the patterns shown in the wavelet map suggest that a typical cycle consists of two distinct phases: (i) gradual growth of large-scale structures in the separated shear layer, accompanied by a progressive growth of the separation bubble, (ii) shedding of a large-scale structure followed by a "collapse" of the bubble and abrupt shortening of the reattachment length.

4. Concluding remarks

Large eddy simulations of the high Reynolds number ($Re_d = 50,000$) separated-reattaching flow over a bluff rectangular plate have been performed with three subgrid-scale models. The mean flow and turbulence statistics obtained with the selective-structure function model provide very good agreement with the pulsed-wire experimental data obtained at the same Reynolds number and blockage ratio in low free-stream turbulence.

Although the Smagorinsky model yields a mean reattachment length in good agreement with experiments, the turbulence statistics and dynamics of the flow are deficient. Both this model and the structure function model delay the break-up and three-dimensionalization of the separated shear layer. Further downstream, where turbulent transport is largely dominated by large-scale unsteadiness, the Smagorinsky model subgrid-scale dissipation is insufficient, allowing the persistence of small-scale turbulent motion, whereas the structure-function model is too dissipative.

The localization achieved with the selective structure function model yields lower time-averaged subgrid-scale dissipation and results in dynamic features of separation and reattachment that compare well with flow visualization. With the λ_2 technique, the large-scale structures in the reattachment region are clearly identified as horseshoe vortices. The characteristic frequencies and intermittent nature of the pseudo-periodic vortex shedding from the separated shear layer and the reattachment region, as well as the shear layer flapping were captured in the simulations.

Acknowledgements

The authors benefited from very stimulating discussions with Dr. Henri Boisson (IMFT, Toulouse) during the course of this work. The financial support of the Natural Sciences and Engineering Research Council of Canada (NSERC) is gratefully acknowledged.

References

Cherry, N.J., Hillier, R., Latour, M.E.M.P., 1983. The unsteady structure of two-dimensional separated and reattaching flows. J. Wind Eng. Ind. Aero. 11, 95–105.

Djilali, N., Gartshore, I.S., 1991a. Turbulent flow around a bluff rectangular plate. Part I: Experimental investigation. ASME J. Fluids Eng. 113, 51–59.

Djilali, N., Gartshore, I.S., 1991b. Turbulent flow around a bluff rectangular plate. Part II: Numerical Predictions. ASME J. Fluids Eng. 113, 60–67.

Farge, M., 1992. Wavelet transform and their application to turbulence. Ann. Rev. Fluid Mech. 24, 395–457.

Ferziger, J.H., 1993. Large-Eddy Simulation of Complex Engineering and Geophysical Flows. Cambridge University Press, New York, pp. 19–33.

Hillier, R., Cheery, N.J., 1981. The effect of stream turbulence on separation bubble. J. Wind Eng. Ind. Aero. 8, 49–58.

Jeong, J., Hussain, F., 1995. On the identification of a vortex. J. Fluid Mech. 285, 69–94.

Jeong, J., Hussain, F., Schoppa, W., Kim, J., 1997. Coherent structures near the wall in a turbulent channel flow. J. Fluid Mech. 332, 185–214.

Kiya, M., Sasaki, K., 1983. Structure of a turbulent separation bubble. J. Fluid Mech. 137, 83–113.

Kiya, M., Sasaki, K., 1985. Structure of large-scale vortices and unsteady reverse flow in the reattaching zone of a turbulent separation bubble. J. Fluid Mech. 154, 463–491.

Kogaki, T., Koyayashi, T., Taniguchi, N., 1997. Large-eddy simulation of flow around a rectangular cylinder. Fluid Dynamics Res. 20, 11–24.

Le, H., Moin, P., Kim, J., 1998. Direct numerical simulation of turbulent flow over a backward facing step. J. Fluid Mech. 330, 349–374.

Lesieur, M., Métais, O., 1996. New trends in large-eddy simulations of turbulence. Ann. Rev. Fluid Mech. 28, 45–82.

Mason, P.J., Callen, N.S., 1986. On the magnitude of the subgrid-sacle eddy coefficient in large-eddy simulations of turbulent channel flow. J. Fluid Mech. 162, 439–462.

Saathoff, P.J., Melbourne, W.H., 1997. Effects of free stream turbulence on surface pressure fluctuations in a separation bubble. J. Fluid Mech. 337, 1–24.

Silveira, N.A., Grand, D., Métais, O., Lesieur, M., 1993. A numerical investigation of the coherent structures of turbulence behind a backward-facing step. J. Fluid Mech. 256, 1–25.

Suksangpanomrung, A., Moinat, P., Djilali, N., 1997. Large-eddy simulation of flow over abluff plate. In: Proceeding of the CFD97, Vic., pp. 255–262.

Suksangpanomrung, A., 1999. Investigation of unsteady separated flow and heat transfer using direct and large-eddy simulations. Ph.D. Thesis, University of Victoria, Department of Mechanical Engineering.

Tafti, D.K., Vanka, S.P., 1991. A three-dimensional numerical study of flow separation and reattachment. Phys. Fluids A 3 (12), 2887–2909.